AIAA JOURNAL
Vol. 39, No. 11, November 2001

Detection of Multiple Damages by Prestack Reverse-Time Migration

X. Lin* and F. G. Yuan†
North Carolina State University, Raleigh, North Carolina 27695

An approach to detect and image multiple damages in a platelike structure is presented. A structural health monitoring system (SHMS) with a linear array of actuators/sensors is proposed. The integrated actuators/sensors are used to activate/receive lowest-order antisymmetric A_0 mode Lamb waves. A migration technique used in geophysical exploration and seismic prospecting is adopted to interpret the backscattering wave field and to image the flaws in the structure. The proposed approach is modeled by a two-dimensional explicit finite difference method both in simulating the reflection waves and in implementing the prestack migration. An analytical solution based on Mindlin plate theory (Mindlin, R. D., "Influence of Rotary Inertia and Shear on Flexural Motions of Isotropic, Elastic Plates," *Journal of Applied Mechanics*, Vol. 18, No. 1, 1951, pp. 31–38) is derived to verify the accuracy of the numerical algorithm. An excitation-time imaging condition specifically for the migration of waves in a plate is introduced based on a ray tracing concept, and prestack reverse-time migration is proceeded to propagate the reflection energy back to the damages. The plate is imaged in terms of the velocity of transverse deformation after migration, thus, the locations, dimensions, and seriousness of the flaws can be visually displayed. Numerical results show that multiple damages can be successfully detected and the image of the damages correlate well with the target damages. The conclusion is that prestack migration can be a prospective technique in SHMS applications.

Nomenclature

C_0	=	velocity of extensional waves in a plate, $\sqrt{[2/(1-\nu)]}C_s$
C_s	=	velocity of shear waves, $\sqrt{(G/\rho)}$
D	=	plate bending stiffness, $Eh^3/[12(1-\nu^2)]$
E	=	Young's modulus
f_0	=	central frequency of the excitation signals
G	=	shear modulus
h	=	plate thickness
M_r, M_θ	=	bending moment
N_p	=	peaks of the excitation signals
P	=	amplitude of the transverse loading
Q_r, Q_θ	=	shear force
q	=	transverse loading
r	=	distance between a sensor and an actuator
w	=	transverse displacement
Δs	=	grid space for both x direction and y direction, Δx and Δy, respectively.
Δt	=	time step
κ	=	shear correction factor, $\kappa^2 = \pi^2/12$
λ	=	wavelength
ν	=	Poisson's ratio
ρ	=	mass density
ω	=	angular frequency, $2v = 2\pi f$

I. Introduction

THE integrity of structures such as aircraft needs to be monitored constantly to prevent catastrophic failures. To respond to any possible damage leading to the failure of structures, damage should be detected, evaluated, and, if possible, monitored, even though the structures might be in service. Traditional nondestructive testing/evaluation (NDT/NDE) techniques cannot be directly applied to monitor structures' health status because these techniques usually are based on in-laboratory testing and require bulky instruments. Especially for aerospace vehicles, the health monitoring is required to perform on in-service structures without manual interference. Thus, developing structural health monitoring systems (SHMS) that can be integrated into the structures as a built-in active diagnosis system has attracted more attention.[1–13] Regarding the potential applications, the research topics can be divided into two major categories: integrating optimized actuators/sensors into structures and developing robust diagnosis algorithms.[1] Strain gauges, piezoelectrics, optical fibers, and PVDF have been studied and implemented in SHMS functioning as actuators or sensors.[2–5] The diagnosis algorithms, which are dependent on the physical signal category determined by an actuator/sensor system, cover a wide range as well, from conventional techniques, such as modal analysis, optimization method, etc., to artificial intelligence related techniques, such as fuzzy logic, neural networks, etc.[6,7] Among these research topics, generating and interpreting wave signals is the focus of much current research due to some unparalleled advantages of this technique.[8]

Guided waves in structures can propagate a long distance; thus, they are very suitable to be utilized in health monitoring for large-area structures like wings and fuselages. They can detect not only the damages on the surface of the structures, but also the flaws inside the structures. The detectability of smaller sized damage can be obtained simply by increasing the frequency of diagnostic signals. The generating and collecting wave signals are readily accommodated through the distributed actuator/sensor system. The difficulty of applying ultrasonic waves based monitoring in SHM is to interpret the received signals given their dispersive properties and complicated mode conversion phenomena. Preliminary methods of interpreting ultrasonic signals include comparing some characteristic parameters, such as wave speed, arrival time, and amplitude in the time domain between virgin structures and damaged structures, and drawing conclusions based on the comparison results. Frequency-domain analysis, such as spectrogram, wavelet, and time-frequency distribution, has also been applied to damage detection. These methods can only recognize the existence of the damage and cannot provide quantitative information about the damage. One reason might be that a unique solution cannot be obtained in an inverse problem of extracting the system's parameters from the system's output.

Recently, many researchers have attempted to propose methods from either the hardware or software prospective to propagate the received reflection waves back to the reflector (damage) and, thus, realize quantitative damage detection. Fink[9] used up to 128 piezoelectric transducers to generate and receive sound waves. The wave signals were stored in memory and read backward to constitute a reverse wave field. The reversed waves were then reemitted to detect the flaws by focusing the waves. By using this so-called time reversal

Received 13 February 2000; revision received 31 October 2000; accepted for publication 6 April 2001.

*Research Assistant, Department of Mechanical and Aerospace Engineering.

†Professor, Department of Mechanical and Aerospace Engineering. Senior Member AIAA.

mirror, he could identify a flaw with dimensions as small as 0.4 mm. The disadvantage of this technique is that it is based on point-by-point testing and might not be applicable in SHMS. Deutsch et al.[10] also used the concept of reversing the reflection field. A linear array was used to focus both Rayleigh waves and Lamb waves. The time of flight was estimated through the cross correlation of reemitted and received signals. The array was self-adjusted by a delay of calculated time of flight, and the received signals were sent out again to amplify the reflection. By iterative operation of this procedure and switching the element as transmitter, the ultrasonic signals were illustrated numerically and experimentally to be able to focus on an artificial anomaly in an aluminum plate. Liu et al.[11] indicated that the migration could be applied in the nondestructive evaluation for concrete structures. In their studies, a surface crack was assumed a priori; thus, all of the imaging processes were simplified to find the first arrival time and convert it into the distance by timing the wave propagation velocity. In a previous study by the authors,[12] a poststack migration technique was used to interpret the wave field. Surface-mounted piezoelectric disks on both sides of the plate were arranged as a linear array and were used to act as both actuators and sensors. The actuators excite lowest-order antisymmetric A_0 mode Lamb waves, and the sensors collect the waves reflected from the damage. This procedure is analogous to the data acquisition experiment in geophysical exploration. Thus, migration, which is an advanced technique in geophysics and seismology,[13–16] could be used to process the data in SHM. The migration technique treats the reflector (damage) as a secondary source, and the problem becomes one of inversely tracing a source that can be uniquely determined. Several data processing procedures, such as normal moveout correction, deconvolution, and muting, that are related to poststack migration were also discussed. In that study, the one-way wave equation was derived based on the characteristic analysis of Lamb wave propagation. The received reflection wave field was reversed first, then was applied to a finite difference algorithm as time-dependent boundary conditions to backpropagate the wave field. A single damage in the plate was correctly imaged through one-way wave equation based migration. Chien[17] also attempted to adopt the migration technique into damage detection. In his study, the problem was modeled by the classical plate theory, and primitive results were provided. Both the studies in Ref. 12 and in Ref. 17 substantiated that poststack is a very useful method to image the structures. However, this method is based on an exploding reflector model assumption in which the stacking process before migration will destroy the information in the wave field relating to the source-reflector distance and the reflection amplitude. Furthermore, it cannot accurately image dip damages where the surface of the damage is not parallel to the sensor array. In the previous studies, only single and symmetric damages were studied.

The current study attempts to deepen our understanding of damage detection by using prestack migration to image multiple damages. The basic concepts of migration technique were introduced in authors' previous paper[12] and will not be repeated in the current work. Thus, only the basic steps of using prestack migration to interpret the reflection waves are discussed. The objective of this paper aims at detecting two small flaws as a representative illustration in a plate using the prestack migration technique. First, a two-dimensional explicit finite difference algorithm used both for simulating the reflection wave field and implementing the reverse-time migration is briefly reviewed. An analytical solution based on Mindlin plate theory[18] is derived to verify the accuracy of the simulation. An excitation-time-based imaging condition is proposed from a two-dimensional ray equation and is simplified by asymptotic analysis of the wave velocity. A correction is applied to the imaging condition to compensate for the dispersive effect of Lamb waves. Finally, several migration images of numerical experiments are presented. The good correlation, both on location and dimensions, between imaged damage and target damage validates the feasibility of the proposed technique.

II. Verification of Finite Difference Algorithm

Based on Mindlin plate theory,[18] the flexural waves propagating in a homogeneous, isotropic elastic plate can be described by a governing equation in first-order matrix form:

$$\boldsymbol{E}_0\frac{\partial \boldsymbol{u}}{\partial t} = \boldsymbol{A}_0\frac{\partial \boldsymbol{u}}{\partial x} + \boldsymbol{B}_0\frac{\partial \boldsymbol{u}}{\partial y} + \boldsymbol{C}_0\boldsymbol{u} + \boldsymbol{q} \tag{1}$$

where

$$\boldsymbol{u}^T = \{\dot{w}, \dot{\psi}_x, \dot{\psi}_y, Q_y, Q_x, M_x, M_y, M_{xy}\}$$

$$\boldsymbol{q}^T = \{q, 0, 0, 0, 0, 0, 0, 0\}$$

Matrices $\boldsymbol{A}_0$, $\boldsymbol{B}_0$, $\boldsymbol{C}_0$, and $\boldsymbol{E}_0$ are listed in Ref. 12 and, thus, are not repeated here.

Bayliss et al.[19] proposed an explicit finite difference algorithm that is second-order accurate in time and fourth-order accurate in space. This algorithm can be used to solve a hyperbolic differential equation that has a form like Eq. (1). The details of applying this algorithm to simulate the flexural waves in a plate were discussed in Ref. 12. Attention should be paid to the stability condition of the algorithm

$$\Delta t \le 2\Delta s \Big/ \sqrt{\frac{9E(1-\nu)}{\rho(1+\nu)(1-2\nu)}} \tag{2}$$

To ensure that the simulation error is less than 1% with the second-order accuracy in time and sixth-order accuracy in space,[20] a criterion for selecting optimal grid space can be expressed based on the dispersion relation as

$$\Delta s = \left[\frac{h^2\left(\kappa^2 C_s^2 + C_0^2\right)}{50\left(4h^2 f_0^2 - C_s^2\right)} + \frac{h}{50 f_0}\right. \times \left.\sqrt{\frac{\kappa^2 C_s^4\left(\kappa^2 h^2 f_0^2 + C_0^2\right) + h^2 f_0^2 C_0^2\left(C_0^2 - 2\kappa^2 C_s^2\right)}{\left(4h^2 f_0^2 - C_s^2\right)^2}}\right]^{\frac{1}{2}} \tag{3}$$

To verify the accuracy of the numerical calculation, an analytical solution for the Mindlin plate problem[18] is derived. In a polar coordinate system, the governing equations for axially symmetric wave motions generated by a point force $\tilde{q}(\omega)$ at $r = 0$ are given in the frequency domain by

$$\tilde{M}_r = D\left(\frac{\mathrm{d}}{\mathrm{d}r} + \frac{\nu}{r}\right)\tilde{\psi}_r \tag{4a}$$

$$\tilde{M}_\theta = D\left(\nu\frac{\mathrm{d}}{\mathrm{d}r} + \frac{1}{r}\right)\tilde{\psi}_r \tag{4b}$$

$$\tilde{Q}_r = \kappa^2 Gh\left(\tilde{\psi}_r + \frac{\mathrm{d}\tilde{w}}{\mathrm{d}r}\right) \tag{4c}$$

$$\left(\frac{\mathrm{d}}{\mathrm{d}r} + \frac{1}{r}\right)\tilde{M}_r - \frac{\tilde{M}_\theta}{r} - \tilde{Q}_r = -\frac{\rho\omega^2 h^3}{12}\tilde{\psi}_r \tag{5a}$$

$$\left(\frac{\mathrm{d}}{\mathrm{d}r} + \frac{1}{r}\right)\tilde{Q}_r = -\rho\omega^2 h\tilde{w} \tag{5b}$$

where

$$\tilde{g}(r,\omega) = \int_{-\infty}^{+\infty} e^{-i\omega t} g(r,t)\,\mathrm{d}t$$

where g represents any of the M_r, M_θ, Q_r, ψ_r, and w. Substituting Eq. (4) into Eq. (5), we obtain two equations of motion, each relating plate displacement $\tilde{w}$ and rotation $\tilde{\psi}_r$. By eliminating $\tilde{\psi}_r$ from the two equations, we can get an exclusive equation for transverse displacement $\tilde{w}$:

$$(\nabla^4 + A\nabla^2 + B)\tilde{w}(r,\omega) = 0 \tag{6}$$

where

$$\nabla^2 = \frac{\mathrm{d}^2}{\mathrm{d}r^2} + \frac{1}{r}\frac{\mathrm{d}}{\mathrm{d}r}$$

$$A = \left(\frac{\rho h^3}{12D} + \frac{\rho}{\kappa^2 G}\right)\omega^2, \qquad B = \left(\frac{\rho^2 h^3}{12\kappa^2 G D}\omega^2 - \frac{\rho h}{D}\right)\omega^2$$

When two positive real numbers k_1 and k_2 are defined,

$$k_1^2 = \left(\sqrt{A^2 - 4B} + A\right)/2, \qquad k_2^2 = \left(\sqrt{A^2 - 4B} - A\right)/2$$

The solution of $\tilde{w}$ can be expressed as

$$\tilde{w} = C\left[H_0^{(2)}(k_1 r) - H_0^{(2)}(-ik_2 r)\right] \tag{7}$$

in which constant C could be determined by the applied loading condition. The transverse shear $\tilde{Q}_r$ can be written in terms of $\tilde{w}$:

$$\tilde{Q}_r = \frac{\rho h \omega^2}{B}\left[\frac{\mathrm{d}^3}{\mathrm{d}r^3} + \frac{1}{r}\frac{\mathrm{d}^2}{\mathrm{d}r^2} + \left(A - \frac{1}{r^2}\right)\frac{\mathrm{d}}{\mathrm{d}r}\right]\tilde{w} \tag{8}$$

For a small cylinder with its center at the loading point and its radius $r = a$, by the equilibrium relation of the shear force $\tilde{q}(\omega) = 2\pi a \tilde{Q}_r|_{r=a}$, the constant C can be evaluated by

$$C = \frac{iB\tilde{q}}{4\rho h\omega^2\left(k_1^2 + k_2^2\right)} \tag{9}$$

For a Kirchhoff thin plate, the rotatory inertia and the shear deformation are ignored; thus $A = 0$, $B = -\rho h\omega^2/D$, and $k_1^2 = k_2^2 = k^2 = B$. The solution to classical plate theory (CPT) is then obtained as

$$\tilde{w} = (-i\tilde{q}/8Dk^2)\left[H_0^{(2)}(kr) - H_0^{(2)}(-ikr)\right] \tag{10}$$

The transverse displacement can be obtained by inverse Fourier transform of Eqs. (7) and (10).

The derived solution is first compared to the widely accepted Medick's CPT solution[21] for the purpose of showing that the current reduced solution for CPT is consistent with Medick's solution. Figures 1 show the transient response of transverse displacement at $r = 6$ in. (15.24 cm) of both solutions. In the calculation of Figs. 1, material is chosen as an Al-6061 plate with $h = 0.063$ in. (0.16 cm), $E = 10{,}523$ ksi (72.5 GPa), $\nu = 0.3$, and $\rho = 5.262$ slugs/ft^3 (2710 kg/m^3). The time history of the point force was given by

$$q(r = 0, t) = P[H(t) - H(t - \beta)] \tag{11}$$

where $H(t)$ is a Heaviside step function and the duration time of applied force $\beta = 10\ \mu$s. The transverse displacement of Medick's solution[21] is given by

$$w(r,t) = \begin{cases} \dfrac{Pt}{4\pi\sqrt{\rho h D}} M\left(\sqrt{\dfrac{\rho h}{D}}\dfrac{r^2}{4t}\right) & 0 < t \le \beta \\ \dfrac{P}{4\pi\sqrt{\rho h D}}\left\{tM\left(\sqrt{\dfrac{\rho h}{D}}\dfrac{r^2}{4t}\right) - (t-\beta)M\left(\sqrt{\dfrac{\rho h}{D}}\dfrac{r^2}{4(t-\beta)}\right)\right\} & t > \beta \end{cases} \tag{12}$$

where $M(x)$ is defined as $M(x) = \pi/2 - Si(x) - \sin x + xCi(x)$, and $Si(x)$ and $Ci(x)$ are the sine and cosine integrals, respectively. Both solutions are normalized by

$$\bar{w}(r,t) = \frac{w(r,t)}{P\beta/\left(4\pi\sqrt{\rho h D}\right)} \tag{13}$$

The current CPT solution in Fig. 1a is calculated by Eq. (10). Figure 1a shows good agreement between the current CPT solution reduced from Mindlin plate theory[18] and Medick's CPT solution[21] for the entire period of time. Figure 1b clearly displays the difference between these two approximation theories. For long lengths of time, Mindlin plate theory[18] gives as close results as those by CPT. However, for short times in which the signal is dominated by high-frequency components, the result shows a discrepancy between two

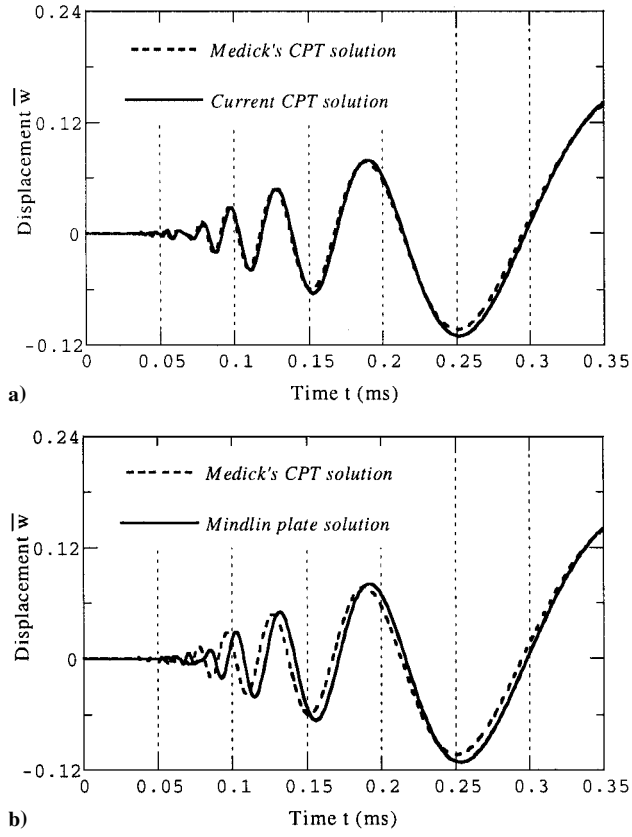

Fig. 1 Transverse displacement at $r = 6$ in. (15.24 cm): a) comparison between Medick's solution[21] and current CPT solution and b) comparison between Medick's CPT solution[21] and Mindlin's solution.[18]

solutions. Further Mindlin solution shows a delay in phase and an increase in amplitude compared with classical theory. This can be explained by realizing that the inertia term in the equation will bring phase lag, and transverse shear deformation will amplify the vertical displacement.

In another study, the excitation of the transient waves is a modulated sinusoid loading governed by

$$q(r = 0, t) = P[H(t) - H(t - N_p/f_0)] \times [1 - \cos(2\pi f_0 t/N_p)]\sin 2\pi f_0 t \tag{14}$$

The waveform of the load ($f_0 = 100$ kHz and $N_p = 5$) and corresponding frequency spectrum are given in Figs. 2a and 2b, respectively.

Figure 3 gives the responses at $r = 6$ in. (15.24 cm) when the plate is subjected to a point load governed by Eq. (14), both from Mindlin plate theory[18] and from CPT. It can be observed that CPT departs distinctly from the Mindlin solution at this frequency (corresponding to $\lambda \approx 7.4h$). When an ultrasonic testing technique is adopted in SHM applications, the order of applicable frequencies ranges from kilohertz to megahertz. Thus, it is necessary to use Mindlin theory or higher-order approximation theory to model the problem.

Figure 4 compares the results based on the derived analytical solution and finite difference result. From Eq. (3) it is clear that the accuracy of finite difference simulation is highly dependent on the wavelength of the propagating waves. In this case, the grid space is

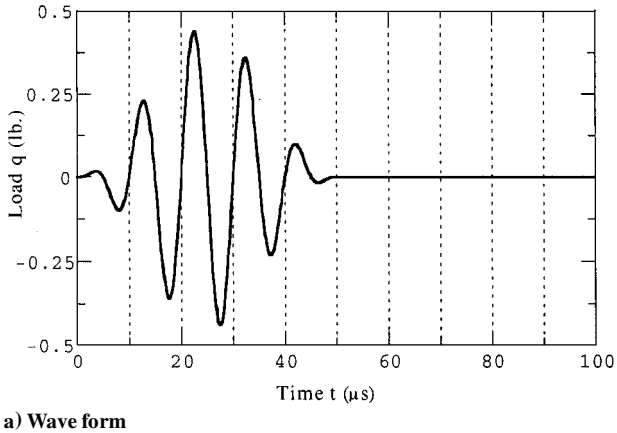

a) Wave form

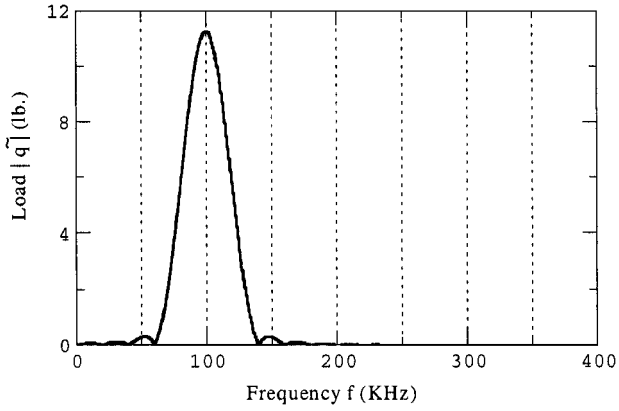

b) Amplitude spectrum

Fig. 2 Loading history and its frequency spectrum.

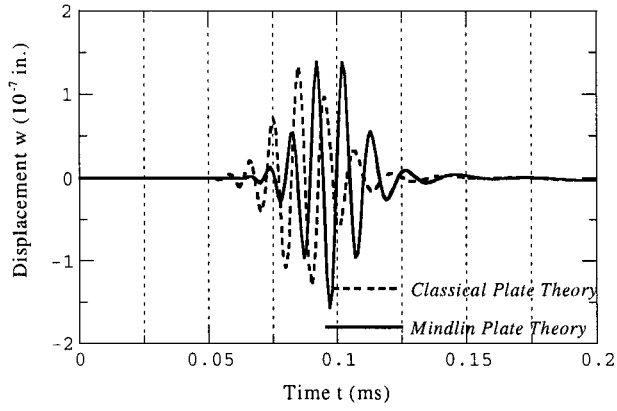

Fig. 3 Comparison of transverse displacements at $r = 6$ in. (15.24 cm) between CPT and Mindlin plate theory[18] when the load is modulated sinusoid function.

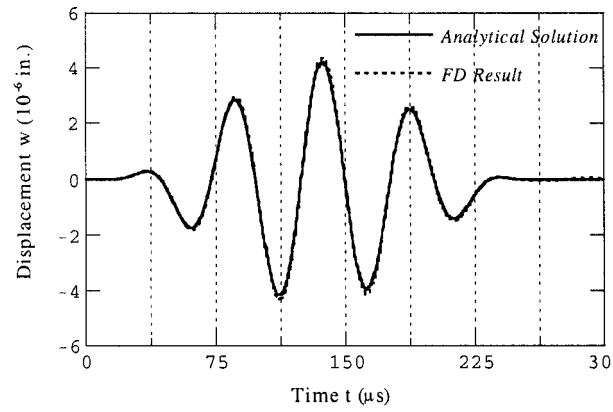

a) $r = 0.4$ in. (1.016 cm), $f_c = 20$ kHz, $\Delta x = 0.02$ in. (0.0508 cm)

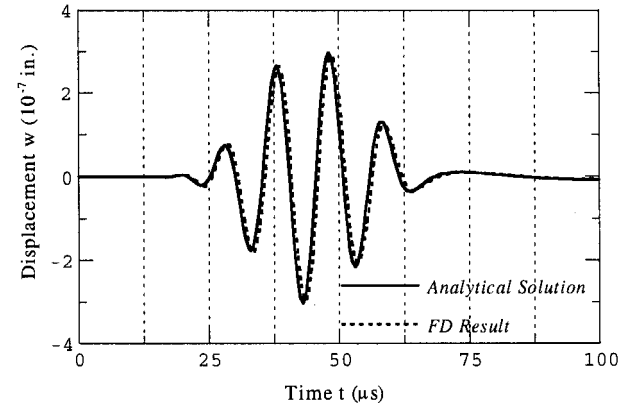

b) $r = 1.6$ in. (4.064 cm), $f_c = 100$ kHz, $\Delta x = 0.02$ in. (0.0508 cm)

Fig. 4 Comparison of transverse displacement between analytical solution (exact Mindlin plate solution[18]) and finite difference result.

chosen as $\Delta s = 0.02$ in. (0.0508 cm). In Fig. 4a, the central frequency is 20 kHz, corresponding to the wavelength $\lambda \approx 17.3h$. This satisfies the requirement that the wavelength should be 10 times less than the grid spacing, thus, the finite difference result agrees well with the analytical solution. Increasing the central frequency while the grid space remains unchanged will decrease the calculation accuracy. As observed in Fig. 4b, when the central frequency is $\lambda \approx 7.4h$, the error between two solutions can be clearly recognized. It can be concluded based on Fig. 4 that the constructed finite difference algorithm is capable of simulating the flexural waves accurately based on Mindlin plate theory.[18]

III. Simulation of Reflection Waves from Damages

To generate the reflection wave field scattered by multiple damages in a plate, the plate is viewed as inhomogeneous materials. Each damage is modeled as a small region of the plate with different material constants. This can be implemented simply by altering the matrix $\boldsymbol{E}_0$ in Eq. (1) without affecting the kernel codes of the finite difference program. With this approach, the boundary conditions at the interfaces between the plate and damages are implicitly satisfied, which makes it easier to model damages with complicated geometry and material properties. A plate with dimension 80×80 in. (203×203 cm) with material properties and geometry shown in Figs. 5 and 6 is studied in the current research. A 200×200 finite difference mesh [$\Delta s = \Delta x = \Delta y = 0.4$ in. (1 cm)] is superimposed on the plate region. The origin of the coordinate system is set at the center of the plate. Two small damages, shown in Fig. 5 as the two small circles, are modeled as point diffractors at (4 in., −16 in.) (10 cm, −41 cm) and (−10 in., −10 in.) (−25 cm, −25 cm), respectively. The equivalent bending stiffness D at the grid points representing the damages is chosen as one-eighth of the plate's bending stiffness. The loading-time history, Eq. (14) with $P = 0.225$ lb (1 N), $f_0 = 40$ kHz, and $N_p = 3$, is applied at the center of the plate. Figure 5 displays a snapshot of the synthesized reflection wave field as a whole view of the plate at $t = 300$ μs. At this time, the wave has hit two damages. In Fig. 5, the amplitude of the velocity of transverse deformation $\dot{w}$ at the grid points is shown as a contour plot. Note that two point diffractors are illuminated by the incident waves sequentially, depending on the distance between the damage location and the loading point. The reflection waves radiate from each damage, acting like waves from a point source. Thus, a damage (or reflector) can be treated as a secondary source, generating waves. This phenomenon is one of the foundations of applying migration technique to detect damage in structures. Another observation from Fig. 5 is that the amplitude of reflection waves is dependent on incidence angle. For the points along the direction of a line connecting a diffractor and the loading point, the amplitude reaches a maximum. The amplitude decreases with the increase of the angle deviating from this direction.

Figure 6 shows the reflection wave field in another form, the so-called time section in geophysics. The abscissa represents the

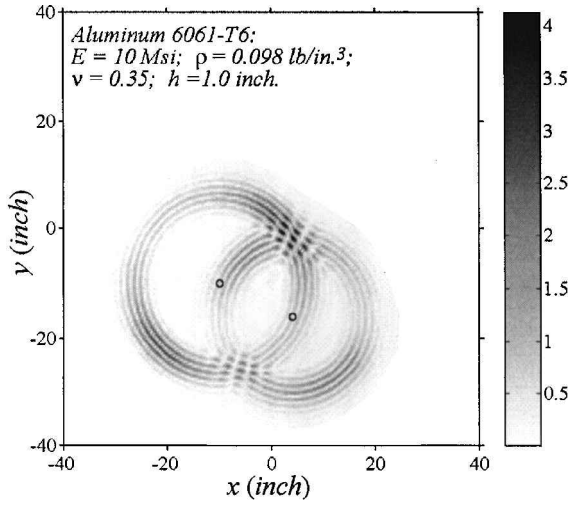

Fig. 5 Snapshot of reflection wave field from two small damages at t = 300 μs.

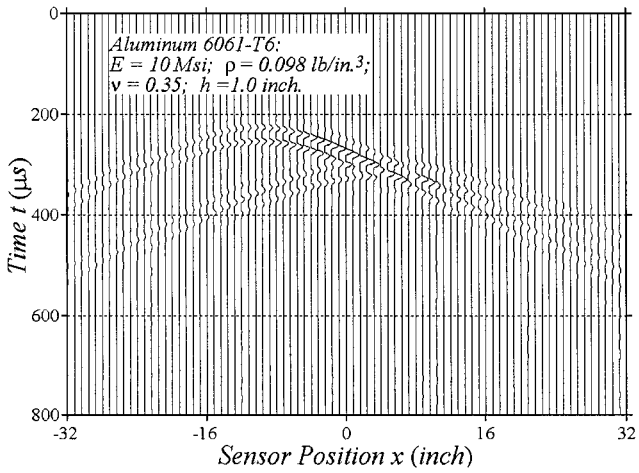

Fig. 6 Time section that is used to execute prestack migration.

position of sensors located at $y = 0$, which is the spatial grid point in the simulation where the waves are recorded. The ordinate represents the propagating time of the waves. Each vertical line (a trace) is a time history of $\dot{w}$ at the corresponding point. For clarity, only every second trace is plotted in Fig. 6. The fluctuation of a line represents the amplitude change of $\dot{w}$. In Fig. 6, the direct arrival of incident waves from the actuator to sensors has been muted by subtracting the received wave field for a plate without damage from the actual wave field with damage. As shown in the Fig. 6, the time span (800 μs) is chosen sufficiently long enough to ensure that all of the sensors can pick up the whole length of the reflection wave package for both point diffractors. Contrary to poststack migration, prestack migration does not impose any restriction that limits on the span of sensors inherited in the normal moveout stacking process. Thus, all of the traces recorded at the points along a horizontal line crossing through the plate could be used to execute the migration. With the increase of the span of sensors, the artifacts in the migration image due to the data truncation can be reduced to a minimum. In this study, the span of sensors is conservatively chosen as from -32 in. to $+32$ in. (-81 cm to $+81$ cm) to avoid the influence from the edges of the plate. The time section provides the information of reflection events in the time domain and is the data form that is practically obtainable in SHMS. Two hyperbolic reflection events can be noticed in Fig. 6. After migration, these two hyperbolic events will be collapsed into two damage locations. The hyperbolic curve with a peak on the left side indicates the reflection wave from a point reflector (-10 in., -10 in.) (-25.4 cm, -25.4 cm) and another reflection wave from (4 in., -16 in.) (10 cm, -41 cm). Thus, through migration, the information of reflection events can be transferred from the time domain to the spatial domain.

IV. Imaging Damages by Prestack Migration

For a distributed actuator/sensor monitoring system, each actuator can excite A_0 mode Lamb waves in the plate. All of the sensors collect the backscattering waves, and a time section such as shown in Fig. 6 is assembled. In poststack migration, the time sections of different excitations are normal moveout corrected and added up to develop a zero-offset section, which is the data form to be used in the migration.[13] This stacking process increases the signal-to-noise ratio and, thus, improves the quality of migration. However, normal moveout correction is based on the assumption that the reflectors are flat layers; thus, poststack migration is only suitable for the case that actuators/sensors are distributed along an array and the interfaces of the flaws are parallel to this array. Furthermore if the recorded signals are transformed into zero-offset before migration, the information of reflection amplitude relating with actuator/sensor distance (offset) might be lost. In this study, time sections without correction (like Fig. 6) from a single excitation are used to execute the migration. The stacking is processed after migration and applied to the migrated images. The most attractive feature of prestack migration is that it releases the limitation of the fixed pattern of distributed actuators/sensors and that it has the potential to detect any shape of damage.

The migration is based on the full-way wave equation rather than the one-way wave equation. In geophysics, most applications use a one-way wave-equation-based migration. The reason is that the receiver is placed on the Earth's surface, and its recorded signal is the upward traveling waves. Then the migration works as downward continuation of the reflection wave field. In SHMS, the actuator may be placed any region of interest on or in the plate, and it can receive reflection energy from any coming direction. Thus, the two-way wave equation has to be used in migration to backpropagate the waves received by the sensors. Another consideration in geophysics when using one-way wave-equation-based migration is to avoid imaging multiple reflection energy. This is not a concern in SHMS because the incipient flaws we are currently interested in are usually small in size, and the structures could be modeled as homogeneous materials in the migration process. In fact, because the locations and dimensions of the damage are unknown before migration is accomplished, it is unlikely that the material distribution will be estimated. One-way wave-equation-based prestack migration might be necessary when the boundaries of the structure need to be taken into consideration. With full-way wave migration for a single flaw, two images will be developed that are symmetrical with respect to the sensor array. To determine uniquely the real location of the flaw, an auxiliary migration along a different direction is necessary.

Reverse-time finite difference migration is used in this study. The same finite difference algorithm used in simulating the reflection waves is used to perform the migration. The time section is reversed with respect to time first. Each trace was treated as a time-dependent boundary condition of transverse deformation velocity $\dot{w}$ at the grid point corresponding to the sensor. Because the finite difference algorithm used is a two-step time splitting method, the time step in migration is twice the time step in synthesizing the wave field. In real applications, the time step for migration is equal to the sampling interval of the A/D device. By the application of the boundary conditions at all sensor locations at each time step, the received reflection waves are backpropagating toward the damage or secondary sources.

Prestack migration uses the finite offset time section; thus, it has different imaging conditions from poststack migration, in which the whole plate is imaged simultaneously at the end of extrapolation. The excitation-time imaging condition proposed by Chang and McMechan[15] is used in this study. The imaging condition is based on a concept that if both the source and the recorded wave are extrapolated, the reflectors exist at the places where these two waves are in phase to each other. By this condition, a point is imaged at its excitation time. Excitation time is defined as the moment when the point is excited by the energy from the actuator. This imaging condition is explicit, and each point in the image space has its own image time. Thus, at each time step $i\,\Delta t$, imaging is processed at all of the grid points located on a locus defined by

$$t_d = (N - i + 1)\Delta t \tag{15}$$

where t_d is the one-way travel time from the loading point to the points and N is the total time steps. The direct arrival time can be obtained by extrapolating the source through a finite difference algorithm. In this study, it was done by an approximation based on ray tracing concepts. Based on Fermat's principle, an arbitrary ray path $\boldsymbol{P}$ in a heterogeneous medium with wave velocity distribution $C(x, y)$ is governed by the ray equation[22]

$$\frac{\mathrm{d}}{\mathrm{d}p}\left[\frac{1}{C(x, y)}\frac{\mathrm{d}x}{\mathrm{d}p}\right] = \frac{\partial C(x, y)}{\partial x} \tag{16a}$$

$$\frac{\mathrm{d}}{\mathrm{d}p}\left[\frac{1}{C(x, y)}\frac{\mathrm{d}y}{\mathrm{d}p}\right] = \frac{\partial C(x, y)}{\partial y} \tag{16b}$$

where $\mathrm{d}x = \mathrm{d}p\cos\theta$ and $\mathrm{d}y = \mathrm{d}p\sin\theta$.

Equation (16) can be further transformed into

$$\frac{\mathrm{d}x}{\mathrm{d}t} = C(x, y)\cos\theta$$

$$\frac{\mathrm{d}y}{\mathrm{d}t} = C(x, y)\sin\theta$$

$$\frac{\mathrm{d}\theta}{\mathrm{d}t} = \frac{\partial C}{\partial x}\sin\theta - \frac{\partial C}{\partial y}\cos\theta \tag{17}$$

The first two equations in Eq. (17) specify the change of ray positions with respect to time, and the third equation specifies the change of ray direction with respect to time. Then, summing the travel time on all of the segments along the ray path gives the direct arrival time

$$t_d = \int_{\boldsymbol{P}} \frac{\mathrm{d}p}{C(x, y)} = \sum_i \frac{\Delta p}{C(x, y)} \tag{18}$$

If the damage dimension is ignored and the plate is considered as homogeneous, θ in Eq. (17) is a constant, which means that the wave front is a circle centering at loading point and a ray path is a straight line along the radius r. It appears that the direct arrival time simply equals $t_d = r/C_d$, where C_d is a wave velocity determined for calculating imaging condition.

If the waves in a plate have a form like $e^{i(\omega t - \gamma r)}$, where γ represents the wave number, the slow flexural wave w_1 and fast flexural wave w_2 can be decoupled from each other by Eq. (5) as

$$\left(\nabla^2 + \gamma_i^2\right) w_i = 0, \qquad i = 1, 2 \tag{19}$$

where

$$\gamma_i^2 = (\rho h\omega^2/2D)\left[\sqrt{(S - R)^2 + 4D/\rho h\omega^2} \pm (S + R)\right]$$

$$R = h^2/12, \qquad S = D/\kappa^2 Gh$$

Thus, the velocities V_1 and V_2 of slow and fast flexural waves are frequency dependent. When frequency is very high, as occurs in ultrasonic testing, it can be shown that

$$V_1 = \omega/\gamma_1 \to \kappa C_s \tag{20}$$

$$V_2 = \omega/\gamma_2 \to \sqrt{[2/(1 - \nu)]}C_s \tag{21}$$

that is, the velocity of slow flexural waves and fast flexural waves approach the velocities of Rayleigh waves and plate extensional waves, respectively. In both numerical simulation and experiments, the arrival of fast flexural waves is hardly discernable. The reason might be that most of the energy is propagating in the velocity of shear waves C_s, which is close to the velocity of slow flexural waves. Thus, in this study, the velocity used to estimate the direct arrival time is approximately chosen as

$$C_d = C_s \tag{22}$$

The imaging condition locus for each extrapolation time step is calculated in advance and used as a reference table in the migration process. At each extrapolation step, those points on which the direct arrival time locus crosses with the backpropagating wave front are imaged in terms of the velocity of transverse deformation $\dot{w}$. The imaging locus does not always cross the grid point. In the current study, a point that is not more than $\Delta s/4$ from the locus was imaged at this time step. One grid point might be imaged more than one time during one time section migration because the stability criterion of finite difference algorithm prevents the locus from passing through one grid space in one time step. The mean value of the imaging variable is used to image these points. On the other hand, all of the loci for all time steps may not cover all of the grid points. Thus, interpolation for the image is necessary. One alternative to applying interpolation is in the process of extrapolation, or interpolation in terms of time step. This will lower the speed of migration and increase the memory requirement of the calculation. Another way to accomplish this is after the whole extrapolation, which means that the interpolation was totally completed in the spatial domain and would turn out a smoother image. To compensate the effect that the waves attenuate over the traveling distance, the image intensity at one point was multiplied by r, which is the distance between that point and the loading point.

Figure 7 displays four snapshots of backpropagating waves in the process of reverse-time migration at four different times. The reflection wave field is generated from two small damages at points A (−10 in., −10 in.) (−25 cm, −25 cm) and B (4 in., −16 in.) (10 cm, −41 cm). The actuator is placed at (−20 in., 0 in.) (−51 cm, 0 cm). The time at which a snapshot is taken is labeled in the caption of each frame, and these times were counted from the recording startup point of the time section. Thus, the real time of each frame counting from the beginning of the migration process should be the time span of the time section (800 μs) minus the labeled time. The dashed line superimposed on each snapshot represents the imaging condition locus (points with constant direct arrival time) at this moment. The two small circles represent the target damage. Figure 7 illustrates how reverse-time migration backpropagates the recorded reflection waves and how the excitation-time imaging condition is applied to image multiple damages. In Fig. 7a, the recorded wave field is extrapolated and begins to propagate toward the damage. The reflected energy from damage A is focused back to its secondary source through migration at time 278 μs (Fig. 7b), where the imaging condition locus is coincident with the wavefront of downward (negative y direction) wave field. The hyperbolic event induced by damage B is collapsed into a point diffractor at the right position at 153 μs (Fig. 7c). In Fig. 7d, the reflection energy continued its downward propagation, and the wavefronts were much like an image of overmigration. The waves propagate divergently and the wavefront would not be coincident with the shrinking imaging condition locus again, thus, no new point would be imaged.

Because the detectability of different damages is strongly dependent on the incidence angle of ultrasonic waves, migration of time sections from a single actuator might not give a complete image of the damages. For distributed actuator/sensor plate structure, each time one actuator is used to excite flexural waves while all of the sensors collect the reflection signals, then a time section is assembled. Applying migration to each time section gives an image of the plate. A complete image could be obtained by adding up all of these images. This stacking process after migration also increases the signal-to-noise ratio. The more actuators used, the higher the signal-to-noise ratio and the better the resolution that can be obtained for the final image. Increasing the times of migration will increase the computation burden, which is not favorable in real time SHM.

V. Numerical Results

This section shows some images obtained by prestack reverse-time migration. The material constants and the dimensions of the plate are given in Fig. 5. The plate, which is discretized by a 200 × 200 finite difference mesh, is imaged at each extrapolation step by extracting the velocity of transverse deformation $\dot{w}$ at each grid point and was displayed as a gray scale contour plot. In Figs. 8–11, the circles with a solid line represent the target damage. In Figs. 8–11, the sensors were assumed to be placed at each grid point along the x axis, ranging from (−32 in., 0 in.) (−81 cm, 0 cm) to (32 in.,

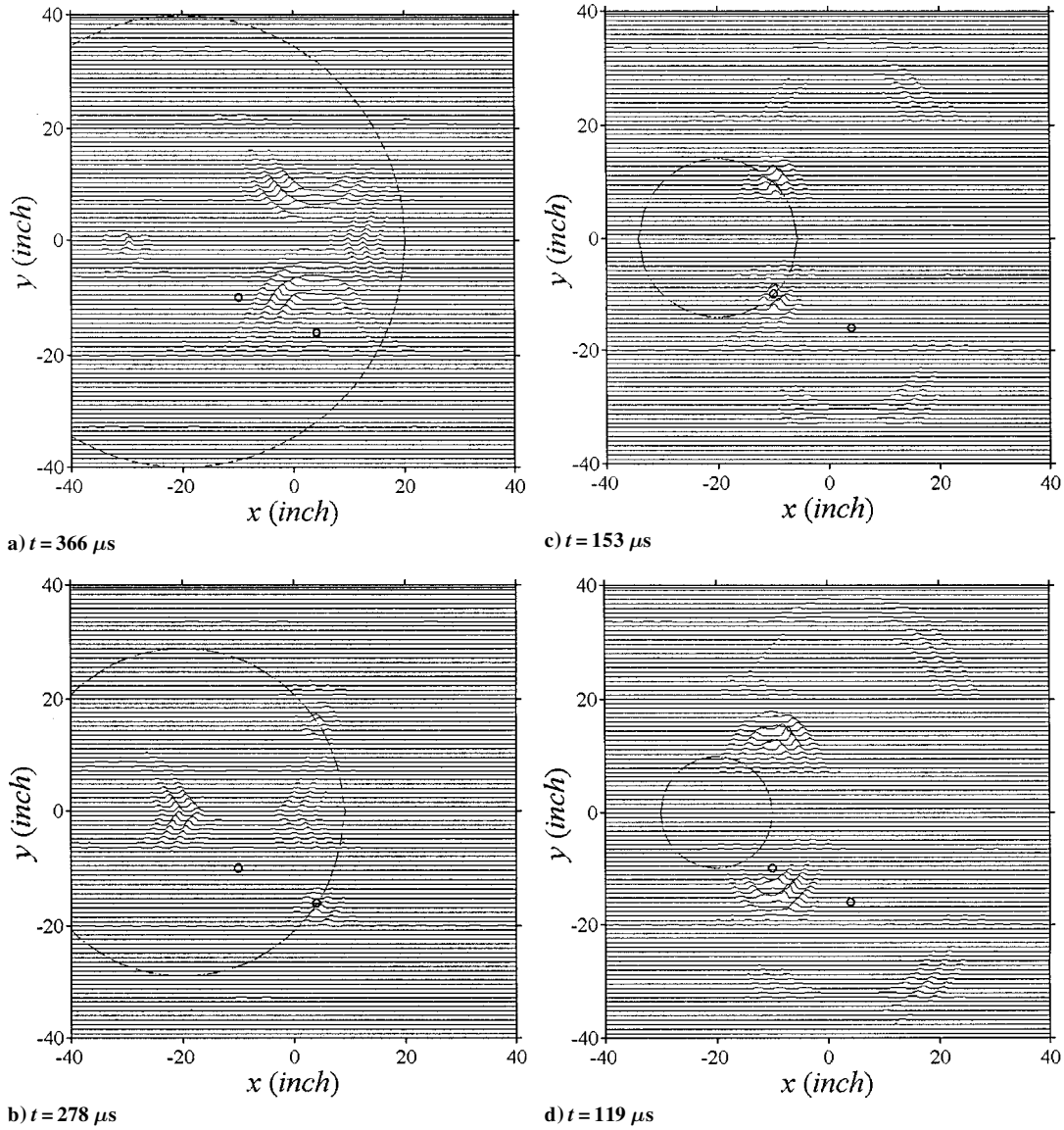

a) $t = 366\ \mu s$ c) $t = 153\ \mu s$

b) $t = 278\ \mu s$ d) $t = 119\ \mu s$

Fig. 7 Snapshots of backpropagating waves in reverse-time migration.

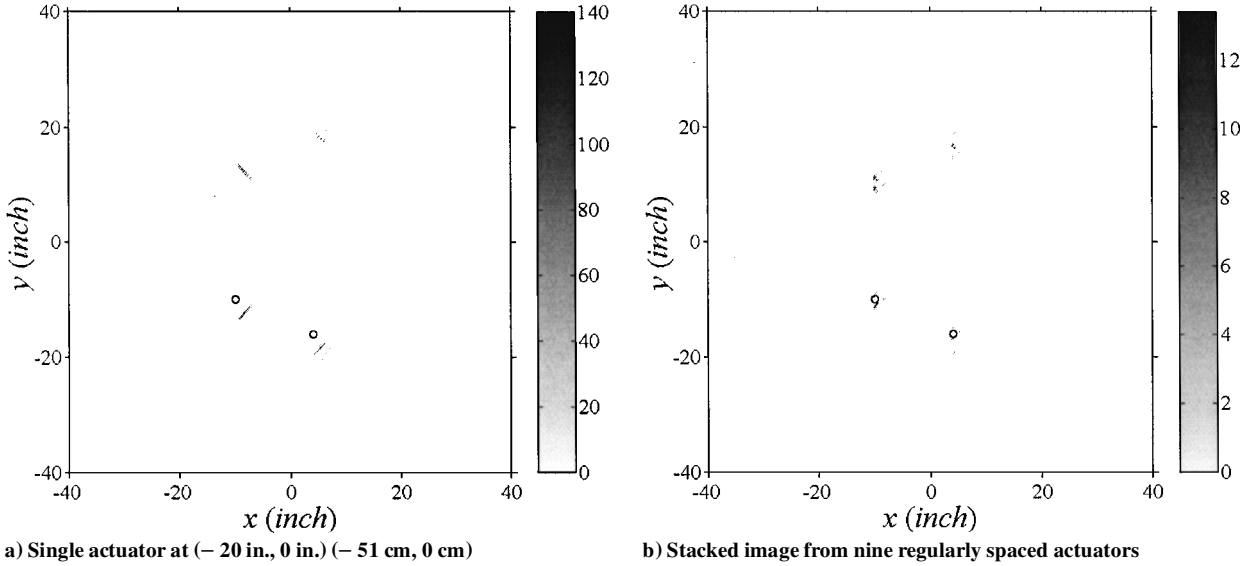

a) Single actuator at (− 20 in., 0 in.) (− 51 cm, 0 cm) b) Stacked image from nine regularly spaced actuators

Fig. 8 Images of plate.

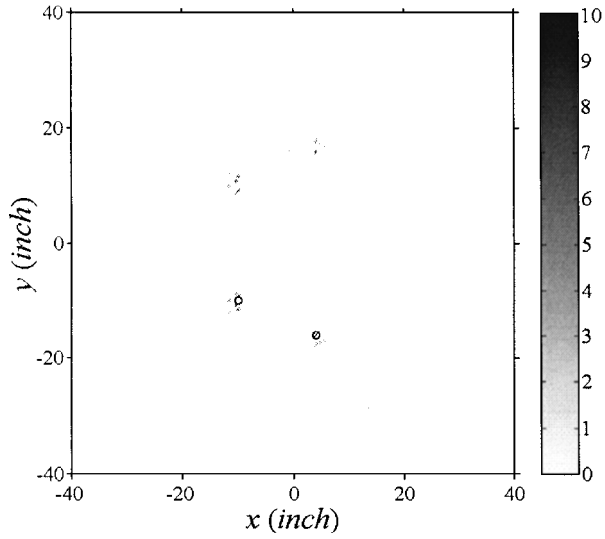

a) Actuator at (0 in., 0 in.) (0 cm, 0 cm)

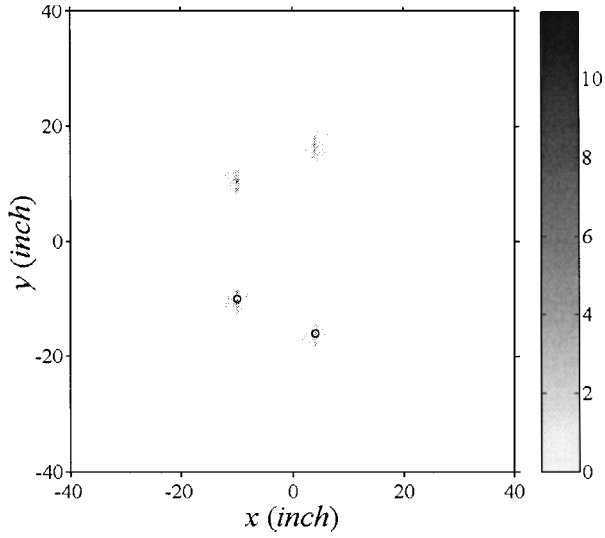

b) Stacked image

Fig. 9 Images of plate, side effect of nonspike excitation was compensated in migration.

0 in.) (81 cm, 0 cm). Nine of the sensors also function as actuators, which are located ranging from (−20 in., 0 in.) (−51 cm, 0 cm) to (20 in., 0 in.) (51 cm, 0 cm) with an interval of 5 in. (12.7 cm). Each actuator gives one shot to excite A_0 mode Lamb waves. The traces collected by all of the sensors are used to assemble the time section.

Figure 8 gives an example of migration images. Figure 8a is the image migrated from a single shot generated by an actuator located at (−20 in., 0 in.) (−51 cm, 0 cm). Figure 8b is the image stacked from migration images of nine actuators' time sections. Figures 8a and 8b show that the prestack migration successfully propagated the reflection energy back to the secondary sources, and two damages are clearly shown in the plate image. The locations of the damage's images are very close to the real locations of target points, although there were some small discrepancies for the dimensions, shapes, and locations between result images and real damages. The errors might result from the use of a narrowbanded excitation signal. To obtain a perfect image, the excitation should be a spike signal to ensure a high resolution. Because of Lamb waves' dispersive properties, a widebanded signal will distort progressively during propagation. Thus, a narrowbanded signal is used as excitation. In this study, the narrowbanded waves had not been deconvoluted, the duration time of the source wavelet would worsen the image. After the traces are reversed in time, an endpoint of the source wavelet package actually becomes a wave front during the migration progress. Thus, the wave front imaged according to excitation imaging condition is

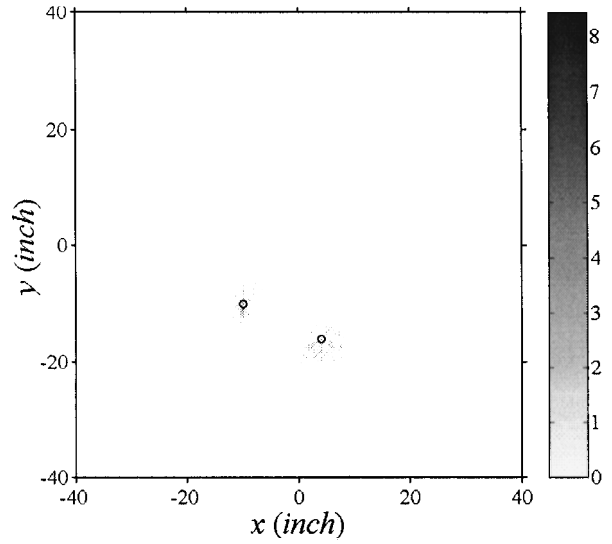

Fig. 10 Stacked image from one-way wave equation based migration.

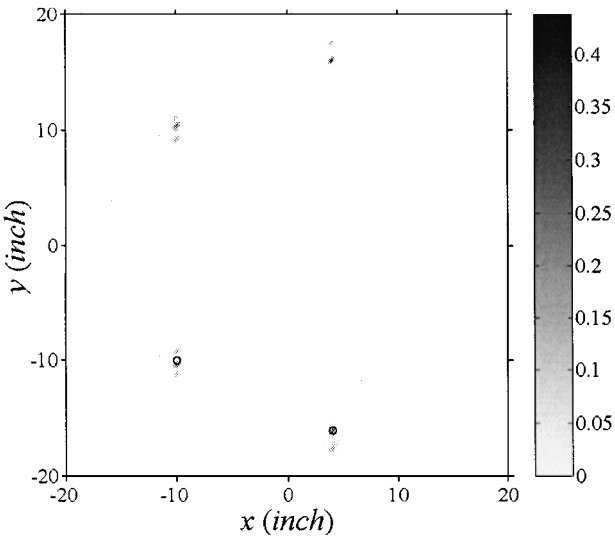

a) Stacked from nine images

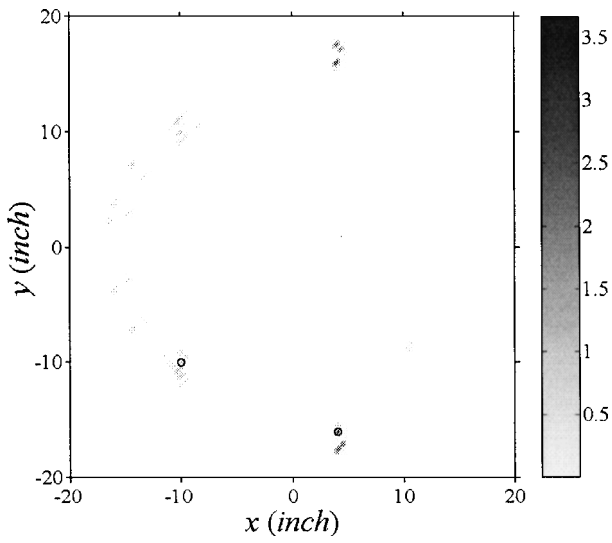

b) Stacked from three images

Fig. 11 Images of plate, migration was performed from a small number of actuators/sensors.

not a real front, and there is a deviation by the value of duration length of the source package. This will also introduce an error to the location of imaged damages. From the results, it is observed that there is a strong direction dependence of the images (stronger in the direction of wave front propagation), which resulted from a diffractor's reflection amplitude being angle dependent. When Figs. 8a and 8b are compared, it is evident that the image after stacking has much better quality than the image from a single shot. It is expected that the stacking process will also suppress the effect of real noise and improve the performance of the migration, which will be pursued in future experimental studies. However, note that the time required to carry out the prestack migration for N time sections of N actuators is N times that for single shot, which is not favored in real-time monitoring.

Figure 9 shows in the migration images that the side effect of nonspike excitation is compensated. Figure 9a is the image from a shot initiated by the actuator at the center of the plate. The stacked image from nine shots is shown in Fig. 9b. For compensating the location error caused by the nonspikelike source wavelet, half of the duration time of the wavelet is subtracted from the direct arrival time in the calculation of the imaging condition table. The resultant images in Fig. 9 show that the image quality is much improved after compensation. The images of the damage overlapped the targets more accurately than the images in Fig. 8. The effect of image's angle dependence on the source position is also weakened.

Figure 10 shows a stacked image of the plate obtained from the one-way wave-equation-based migration. An equation for downward (negative y direction) propagating waves is used.[12] As shown in Figs. 8 and 9, in the two-way wave migration a pseudoimage together with the right image of each damage appeared symmetrically with respect to x axis, along which the sensors are distributed. Because both damages are located below the x axis and, intentionally, downward extrapolation is chosen, the resultant image shows the correct locations of damages, and no pseudoimage appeared. In this case, a damage located above the x axis is not imaged. Figure 10 implies that the one-way wave-equation-based migration can be used in SHS only if the sensors were placed along the edge of a plate. It is also observed that there is energy scattered around the target damages. The reason might be that the one-way wave equation used had not been corrected to preserve the dispersion relation of real full-way waves.

Figure 11 displays plate images from migration with fewer actuators/sensors. Nine piezos form a line array ranging from (−24 in., 0 in.) (−61 cm, 0 cm) to (24 in., 0 in.) (61 cm, 0 cm) with a spacing of 6 in. All of the piezos function as sensors. In Fig. 11a, all of the sensors also act as actuators. In Fig. 11b, only the three piezos at (−24 in., 0 in.), (0 in., 0 in.), and (24 in., 0 in.) or at (−61 cm, 0 cm), (0 cm, 0 cm), and (61 cm, 0 cm) are chosen to excite the A_0 mode Lamb waves. It is expected that the fewer the actuators/sensors, the poorer the resolution and the quality of images may result. However, the number of actuators/sensors in a real structural monitoring system should be kept as small as possible so that the monitoring system will not add extra complexity and reduce the strength and performance of the structure. Figure 11 demonstrates that prestack migration is still applicable when very few actuators/sensors are used. The number of sensors is cut down dramatically compared to the Fig. 9 case. The damage imaging quality of both Figs. 11a and 11b is less sharp than that of the stacked image in Fig. 9b, but they both give a clear indication of existing damage. In Fig. 11b, there is a noticeable error for the imaging of the location of target damage. It could be concluded from the comparison among these images that the number of actuators, which determines how many images will be stacked, is more critical than the number of sensors as a factor of affecting accuracy of the damage detection. That the image quality is not deteriorated significantly with few actuators/sensors is an advantage for prestack migration over poststack migration. The reason is that poststack migration is based on a normal moveout corrected section, which is highly dependent on the interval between sensors.

VI. Conclusions

Stress-wave-based prestack migration has been demonstrated numerically to be an advanced technique that could be adopted in an active SHMS. The migration technique serves as a bridge that connects distributed actuator/sensor system and ultrasonic signals and, thus, makes it possible to construct a real-time, automatic, and accurate monitoring system. The prestack migration technique not only can detect the existence of damage, but may also provide information about the dimensions, locations, and seriousness of the damage. It is not necessary to assume a damage pattern before applying prestack migration, which makes it feasible of detecting multiple damages. In this study, damages are modeled as point diffractors, which may not reflect reality. When it is known that every damage with a solid area can be treated as a summation of certain point reflectors, it is believed that prestack migration is capable of detecting any shape and any dimension of the damages. In this paper, a two-way wave equation is suggested to be first choice for prestack migration in SHMS applications. The imaging condition is built based on a general ray equation for two-dimensional heterogeneous materials; thus, it can be extended to structure other than plates. Through an asymptotic analysis of A_0 mode waves, the excitation-time imaging condition is simplified into the direct arrival time of shear waves. After the imaging condition is compensated by a value of half of the duration time of the excitation signal, this imaging condition is proven by the migration results to be an accurate criterion for imaging the extrapolation wave field. The prestack migration technique simplifies the data processing procedures so that the data distortion due to several stacking procedures like normal moveout correction can be avoided. Further more, it has the potential to compensate for the influence of dispersive waves on the accuracy of flaw detection. Overall, prestack migration is a better choice than poststack migration, although prestack migration requires more computation time.

Future study will focus on the experiment verification of the proposed monitoring system. The proposed system may also be extended to the health monitoring of composite structures.

References

[1]Chang, F. K., "Structural Health Monitoring, a Summary Report on the First International Workshop on Structural Health Monitoring," *Proceedings of 2nd International Workshop on Structural Health Monitoring*, Technomic, Lancaster, PA, 1999, pp. xix–xxix.

[2]Monkhouse, R. S. C., Wilcox, P. D., and Cawley, P., "Flexible Interdigital PVDF Transducers for the Generation of Lamb Waves in Structures," *Ultrasonics*, Vol. 35, No. 7, 1997, pp. 489–498.

[3]Subramanian, H., Varadan, V. K., Varadan, V. V., and Vellekoop, M. J., "Design and Fabrication of Wireless Remotely Readable MEMS Based Microaccelerometers," *Smart Materials and Structures*, Vol. 6, No. 6, Society of Photo-Optical Instrumentation Engineers, Bellingham, WA, 1997, pp. 730–738.

[4]Crawley, E. F., "Intelligent Structure for Aerospace: a Technology Overview and Assessment," *AIAA Journal*, Vol. 32, No. 8, 1994, pp. 1689–1699.

[5]Foedinger, R. C., Rea, D. L., Sirkis, J. S., Baldwin, C. S., Troll, J. R., Grande, R., Davis, C. S., and VanDiver, T. L., "Embedded Fiber Optic Sensor Arrays for Structural Health Monitoring of Filament Wound Composite Pressure Vessels," *Proceedings of SPIE: Smart Structures and Materials*, Vol. 3670, Society of Photo-Optical Instrumentation Engineers, Bellingham, WA, 1999, pp. 289–301.

[6]Kudva, J., and Lockyer, A., "Exploiting Smart Technologies for Military Aircraft Applications, Perspectives on Development of a Smart Air Vehicle," AIAA Paper 99-1511, 1999.

[7]Sun, F. P., Chaudhry, Z. A, Rogers, C. A., Majmundar, M., and Liang, C., "Automated Real-Time Structure Health Monitoring via Signature Pattern Recognition," *Proceedings of SPIE: Smart Structures and Materials*, Vol. 2447, Society of Photo-Optical Instrumentation Engineers, Bellingham, WA, 1995, pp. 236–247.

[8]Boller, C., "Fundamentals on Damage Monitoring," LS-205, AGARD, pp. 4.1–4.15.

[9]Fink, M., "Time-Reversal Mirror," *Journal of Physics D: Applied Physics*, Vol. 26, No. 9, 1993, pp. 1333–1350.

[10]Deutsch, W. A. K., Cheng, A., and Achenbach, J. D., "Self-Focusing of Rayleigh Waves and Lamb Waves with a Linear Phased Array," *Research in Nondestructive Evaluation*, Vol. 9, No. 2, 1997, pp. 81–95.

[11]Liu, P. L., Tsai, C. D., and Wu, T. T., "Imaging of Surface-Breaking Concrete Cracks Using Transient Elastic Wave," *NDT&E International*, Vol. 29, No. 5, 1996, pp. 323–331.

[12]Lin, X., Pan, E., and Yuan, F. G., "Imaging the Damage in the Plate with Migration Technique," *Proceedings of 2nd International Workshop on*

Structural Health Monitoring, Technomic, Lancaster, PA, 1999, pp. 731–742.

[13]Claerbout, J. F., "Toward a Unified Theory of Reflection Mapping," *Geophysics*, Vol. 36, No. 3, 1971, pp. 467–481.

[14]Yilmaz, O., and Claerbout, J. F., "Prestack Partial Migration," *Geophysics*, Vol. 45, No. 12, 1980, pp. 1753–1779.

[15]Chang, W. F., and McMechan, G. A., "Reverse-Time Migration of Offset Vertical Seismic Profiling Data Using the Excitation-Time Imaging Condition," *Geophysics*, Vol. 51, No. 1, 1986, pp. 67–84.

[16]Dai, N., Vafidis, A., and Kanasewich, E., "Seismic Migration and Absorbing Boundaries with a One-Way Wave System for Heterogeneous Media," *Geophysical Prospecting*, Vol. 44, No. 4, 1996, pp. 719–739.

[17]Chien, L. S., "In Situ Damage Detection of Plates by the Migration Technique," AIAA Paper 97-1225, 1997.

[18]Mindlin, R. D., "Influence of Rotatory Inertia and Shear on Flexural Motions of Isotropic, Elastic Plates," *Journal of Applied Mechanics*, Vol. 18, No. 1, 1951, pp. 31–38.

[19]Bayliss, A., Parikh, P., Maentrello, L., and Turkel, E., "Fourth-Order Scheme for the Unsteady Compressible Navier–Stokes Equation," AIAA Paper 85-1694, 1985.

[20]Kelly, K. R., Ward, R. W., Treitel, S., and Alford, R. M., "Synthetic Seismograms: a Finite Difference Approach," *Geophysics*, Vol. 41, No. 1, 1976, pp. 2–27.

[21]Medick, M. A., "On Classic Plate Theory and Wave Propagation," *Journal of Applied Mechanics*, Vol. 28, No. 3, 1961, pp. 223–228.

[22]Lee, W. H. K., and Stewart, S. W., *Principles and Applications of Microearthquake Networks*, Academic Press, New York, 1981, Chap. 2.

A. M. Baz
Associate Editor